Divergent urbanization-induced impacts on global surface urban heat island trends since 1980s

Long Li [a], Wenfeng Zhan [a,b,*], Leiqiu Hu [c], TC Chakraborty [d], Zhihua Wang [e], Peng Fu [f], Dazhong Wang [a], Weilin Liao [g], Fan Huang [a], Huyan Fu [a], Jiufeng Li [a], Zihan Liu [a], Huilin Du [a], Shasha Wang [a]

[a] Jiangsu Provincial Key Laboratory of Geographic Information Science and Technology, International Institute for Earth System Science, Nanjing University, Nanjing, Jiangsu 210023, China
[b] Jiangsu Center for Collaborative Innovation in Geographical Information Resource Development and Application, Nanjing, Jiangsu 210023, China
[c] Department of Atmospheric Science, University of Alabama in Huntsville, Huntsville, AL 35899, USA
[d] Pacific Northwest National Laboratory, Richland, WA 99354, USA
[e] School of Sustainable Engineering and the Built Environment, Arizona State University, Tempe, AZ 85287, USA
[f] Center for Environment, Energy, and Economy, Harrisburg University of Science and Technology, PA 17101, USA
[g] Guangdong Key Laboratory for Urbanization and Geo-simulation, School of Geography and Planning, Sun Yat-sen University, Guangzhou, Guangdong 510006, China

ARTICLE INFO

Edited by Jing M. Chen

Keywords:
Surface urban heat island
Thermal remote sensing
Land surface temperature
Data reconstruction
Landsat data

ABSTRACT

Urbanization experiences different speeds and forms under diverse development stages across the globe. However, urbanization-induced impacts on long-term surface urban heat island intensity (I_s) trends across global cities and the regulators of such impacts remain understudied Here we estimate interannual trends in daytime I_s (i.e., urban-rural differences in surface temperatures) across 511 major cities for 1985–2020 using annual averages calculated using reconstructed land surface temperature data derived from >250,000 Landsat thermal images. Our study reveals that the global mean I_s growth rate is 0.156 °C/decade. We further examine I_s change associated with per 1% impervious land growth (denoted as β) in each city throughout the research period and during different periods. The global mean β is 0.018 ± 0.025 °C/% (mean ± 1 standard deviation) for the whole period, with greater values in humid than in arid climates; and the β may change during different periods, e.g., it has more than tripled when urban impervious land exceeds 30%, indicating the spatiotemporally divergent impacts of urbanization on I_s trends across global cities. The spatial variations in β across global cities are well correlated with rural vegetation abundance and precipitation but not with urban population. Among these three factors, rural vegetation abundance possesses the greatest standardized regression coefficient of partial least-squares model, signifying the critical role of biome background in regulating β. The finding implies that future urbanization over densely vegetated regions should be more carefully and strategically planned due to the greater urbanization-induced surface warming effect.

1. Introduction

The world has witnessed widespread urbanization in recent decades (Liu et al., 2020). One of the consequences is the urban heat island (UHI) effect, which is usually characterized by higher temperatures over urban areas than their rural surroundings (Oke, 1982). The UHI can impact weather through modification of surface energy budget and boundary layer dynamics (Kalnay and Cai, 2003; Qian et al., 2022). One consequence of this is the exacerbation of heat extremes (Sun et al., 2014; Wang et al., 2021; Yang et al., 2017), which adversely impacts the lives and health of urban residents. Accurate understanding of the impact of continued urbanization on UHI trends is critical for both understanding urban impact at the local scale and for informing urban planning strategies towards heat mitigations (UNEP, 2021).

The key of examining urbanization-induced impacts on UHI trends lies in the accurate quantification of UHI trends. Satellite-based land surface temperature (LST) overcomes the under-representation of in-situ air temperature measurements over large areas (Zhou et al., 2022) and it

* Corresponding author at: Nanjing University, Xianlin Campus, No. 163 Xianlin Avenue, Qixia District, Nanjing, Jiangsu, 210023, China.
E-mail address: zhanwenfeng@nju.edu.cn (W. Zhan).

has been frequently used to investigate surface UHI intensity (I_s) trends, either for studies at city (Dewan et al., 2021; Meng et al., 2018; Quan et al., 2016), national (Li et al., 2020a; Yao et al., 2018), or global scales (Chakraborty and Lee, 2019; Si et al., 2022; Yao et al., 2019). However, the research periods of investigations of I_s trends have been mostly limited to the recent two decades (i.e., post-2000), mostly due to the lack of high-quality and temporally consistent satellite-derived LST products before 2000. Global cities should possess highly diverse expansion processes due to divergent urbanization rates during different periods. For example, much faster urbanization has been witnessed in the United States before 2000 than afterwards, while China has experienced more rapid urbanization after 2000 (Liu et al., 2020). Such contrasting urbanization processes are expected to cause divergent I_s trends across global cities during different periods (Supplementary Fig. S1). Therefore, long-term LST observations are required to identify such spatio-temporal disparities in I_s trends. The long-term I_s trends (especially for pre-2000s) are potentially derivable with LST data acquired by Landsat-series satellites, as Landsat-series satellites have sampled the thermal status of the earth's surface for approximately four decades. However, Landsat thermal data are characterized by long sampling interval (~16 days) and strongly impacted by cloud contamination and the stripe-gap effect, making the derivation of I_s trends based on Landsat thermal data extremely difficult (Li et al., 2022a). Therefore, variations in the I_s trends since the 1980s across global cities remain unknown.

Increase in urban impervious land can serve as a proxy for urbanization (Gong et al., 2020; Liu et al., 2020). Numerically, the urbanization-induced impacts on I_s trends are usually evaluated as the I_s change associated per 1% urban impervious land (or urban-rural difference in impervious surface percentage, δISP) growth (Li et al., 2021; Li et al., 2022b; Rizvi et al., 2020), denoted here as β. Investigating the pattern and dynamics of β can deepen the understanding of urbanization-induced impacts on I_s trends (Fu and Weng, 2016; Tran et al., 2017). Previous assessments revealed that β reaches 0.020 °C/% in Beijing-Tianjin-Hebei metropolitan region, China, with a warm temperate climate (Li et al., 2022b). By contrast, β is very small (0.001 °C/%) in Karachi, Pakistan, characterized by an arid climate (Rizvi et al., 2020). However, preceding estimations on β are spatio-temporally constrained in individual cities and/or in relatively short periods (often after 2000); and a global pattern of β remains lacking. Furthermore, the daytime absolute I_s (not the I_s trends) has been shown to be jointly regulated by precipitation, vegetation, and urban population (Li et al., 2019; Manoli et al., 2019; Zhao et al., 2014). Whether β is controlled by these three factors and which factor among these exerts the greatest impacts, especially from a global perspective, remain unknown.

Here, we investigate the I_s trends since the 1980s across 511 cities worldwide with reconstructed LST data obtained based on >250,000 Landsat thermal images, with the MODIS LST data used to validate the reliability in depicting the long-term I_s trends. We further combine I_s and impervious surface data to analyze the urbanization-induced impacts on I_s trends (i.e., β) by establishing their temporal relationships. We also use several other datasets (vegetation abundance, precipitation, and population) to examine the associated regulators of β. The findings of this study should help to deepen the understanding of the change in the urban thermal environment due to continued urbanization over the last four decades.

2. Methods

2.1. Study area and data

We focused on the 511 major cities worldwide with an urban area > 200 km^2 in 2018 (Fig. 1a). These cities are distributed in Africa (34 cities), Asia (194 cities), Europe (82 cities), North America (172 cities), Oceania (6 cities), and South America (23 cities). They are typified by various climate types according to the Köppen-Geiger classification scheme (Kottek et al., 2006), including equatorial (52 cities), arid (51 cities), warm temperate (290 cities), and snow (118 cities) climates. These cities have undergone rapid urbanization in recent decades (Gong et al., 2020) and possess remarkable differences in annual mean temperature and annual total precipitation (Fig. 1b). Moreover, large cities also offer more pixels and make them more suitable for statistical analysis than small cities. Therefore, these characteristics should be useful for assessing and understanding the impacts of urbanization on I_s trends and the regulators of such impacts in different background climates.

We employed LST observations from both Landsat and MODIS Terra satellites. Across the 511 major cities, we processed >250,000 LST images acquired from Landsat-5, −7, and − 8 for the period of 1985–2020, with a spatial resolution of ~100 m as well as overpass time of approximately 10:30–12:00 local time. These LSTs were retrieved by a statistical mono-window algorithm and have been demonstrated to possess an acceptable accuracy (Ermida et al., 2020). These Landsat LSTs were used to reconstruct LST time series and to derive the I_s trends for the period of 1985–2020. The MODIS LSTs for the period of 2000–2020 were extracted from the MOD11A2 V6.1 product. The MODIS LST products have a spatial resolution of 1 km and also possess reliable retrieval accuracy (Wan, 2008). The MODIS LSTs were used to validate the LSTs reconstructed from Landsat thermal data in capturing long-term I_s dynamics and I_s trends.

We also processed impervious surface, urban boundary, elevation, land cover type, vegetation abundance, precipitation, and population data. The impervious surface data (http://data.ess.tsinghua.edu.cn/gaia.html) for 1985–2018 were derived from Landsat images and they hold a relatively high overall accuracy (Gong et al., 2020). These data were employed to characterize urban impervious land growth (i.e.,

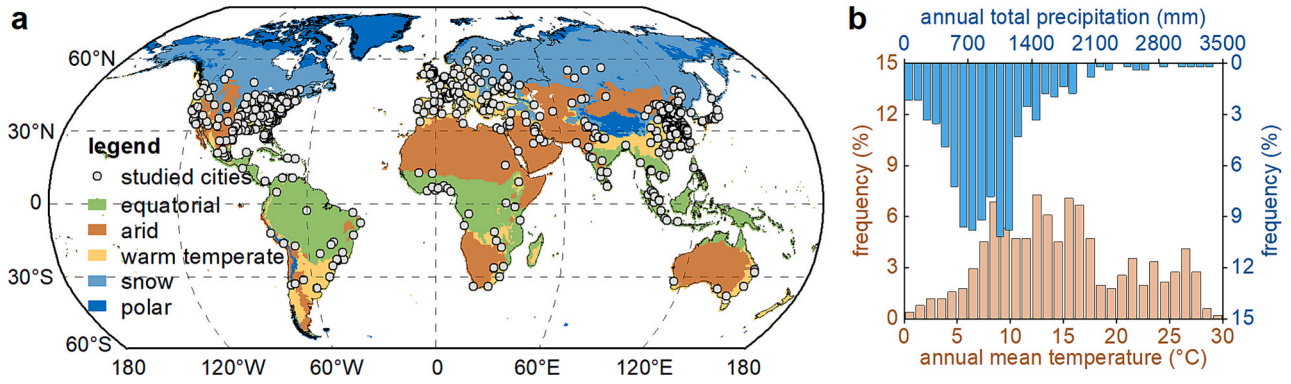

Fig. 1. Spatial distribution and climate characteristics of the 511 studied cities. Distribution of cities and their corresponding climate zones (a) and frequency distribution of annual mean temperature and annual total precipitation (b).

urbanization). The urban boundary data (http://data.ess.tsinghua.edu.cn/gub.html) in 2018 were generated by combining the impervious surface data and a kernel density estimation method (Li et al., 2020b). The urban boundary data were used to delineate urban and rural surfaces. The elevation data were obtained from https://srtm.csi.cgiar.org/. The elevation data possess a spatial resolution of 90 m, and they were applied to suppress the impacts of large elevation variations on the I_s estimation. The land cover type data (https://search.earthdata.nasa.gov/) were obtained from the MCD12Q1 product. They have a spatial resolution of 500 m and were employed to exclude the pixels labeled as 'water', 'wetlands', and 'permanent snow and ice' over urban and rural surfaces. The vegetation abundance data were obtained from the VIPPHEN data product. We retrieved the normalized difference vegetation index (NDVI) in 1985 from VIPPHEN (with a resolution of 0.05°) to examine the impacts from vegetation abundance on β. The reanalysis precipitation data in 1985 were obtained from https://psl.noaa.gov/data/gridded/data.UDel_AirT_Precip.html. The precipitation data (with a resolution of 0.5°) were employed to examine the impacts from precipitation on β. The population data in 1990 (with a resolution of 1 km) were collected from Global Human Settlement Layer (http://data.europa.eu/89h/d6d86a90-4351-4508-99c1-cb074b022c4a). The population data were used to examine the impacts from urban population on β.

We processed all data to a spatial resolution of 1 km for analysis, mainly aiming to match the resolution of LST data and to reduce computational complexity. The continuous (Landsat LST, elevation, vegetation abundance and precipitation data) and discrete (land cover data) variables were resampled by bilinear interpolation and nearest neighbor interpolation, respectively. The impervious surface percentage data were generated based on the proportion of impervious surface within a 1 km^2 rectangle. The MODIS LST and population data preserve their original 1 km resolution. Note that the Landsat LST data were reconstructed at 1 km resolution, mainly because we aim to assess the impacts of urbanization on long-term I_s trends at the city scale and due to the huge data volume involved in reconstructing high-resolution LSTs.

2.2. Estimation of long-term I_s trends using Landsat data

The Landsat LST data cannot be used directly to estimate I_s trends and assess urbanization-induced impacts on I_s trends, due to the long sampling interval (~16 days) and the large differences in data acquisition dates impacted by cloud contamination, stripe gaps, and missing images (Ahmed et al., 2023; Zhou et al., 2019). There is thus a need to reconstruct the Landsat LST with higher spatiotemporal continuity to reduce the sampling bias. The Prophet model can reconstruct data with periodic variability (Taylor and Letham, 2018). The critical capability of the Prophet model is to utilize all available time-series data to simulate the interannual and seasonal dynamics. This model can reduce the sampling bias of LST data arising from cloud contamination, stripe gaps, and missing images by enabling the reconstructed LST dataset with enough values within a year and the relatively consistent dates across years. This method therefore helps estimate LST trends by overcoming the deficiencies of Landsat-derived LST (i.e., with intra-annual periodic variability) time series with severe missing and large differences in acquisition dates (Li et al., 2022a).

Here we employed the Prophet model to reconstruct spatiotemporally continuous Landsat LSTs at 1 km resolution for 1985–2020. The method includes three main steps. We first pre-processed the acquired Landsat LST data by setting all Landsat LST gaps arising from cloud contamination, stripe gaps, and data missing as null values and eliminating LST outliers based on the '3σ (standard deviation)' rule (Lehmann, 2013). With all the pre-processed Landsat LSTs, we then solved for the coefficients of the Prophet model and obtained its interannual, seasonal, and residual components. Using the model coefficients and associated components, we finally generated spatiotemporally continuous LST data under clear-sky conditions across global cities. We compared the Landsat observations with the reconstructed data to evaluate the accuracy of the reconstructed Landsat LST with the mean absolute error (MAE). Note that the LST data were reconstructed at a temporal resolution of 16 days by referring to the revisit period of Landsat satellites. To facilitate understanding, a case in Beijing, China, is presented to show the procedure of the Prophet model to reconstruct Landsat LST (refer to Supplementary Fig. S2).

We delineated the urban areas as the pixels within the urban boundary of 2018 while the rural areas as the buffer zone with an equivalent area to the urban (Zhou et al., 2014). The pixels labeled as 'water', 'wetlands', 'permanent snow and ice', and those pixels with an elevation beyond ±50 m of the urban mean elevation were excluded to suppress their impacts on the I_s estimation (Imhoff et al., 2010; Peng et al., 2012). We then calculated I_s as the difference between the urban and rural mean LSTs:

$$I_s = LST_{\text{urban}} - LST_{\text{rural}} \tag{1}$$

where I_s denotes the surface urban heat island intensity; and LST_{urban} and LST_{rural} denote the urban and rural mean LSTs, respectively.

We estimated the interannual I_s trends for each city using linear regression and tested the significance of I_s trends at the 0.05 level. Only cities with significant I_s trends (i.e., $p < 0.05$) were considered in the global and regional analysis. Considering that we used static urban boundary to estimate I_s, the detected I_s trend mainly reflects the increase in areas affected by I_s due to urban expansion. We further validated the Landsat-derived I_s with those derived from MODIS LST data during 2000–2020. MODIS data have been commonly used to derive I_s trends (Quan et al., 2016; Si et al., 2022; Yao et al., 2018). Thus, the I_s trends derived from MODIS data can be regarded as 'ground truth' under clear-sky conditions, both because of the estimates available from previous studies and also because of the relatively high retrieval accuracy of and high-frequency (i.e., daily) revisit of MODIS LST data (Chakraborty et al., 2021). We assessed the accuracy of the Landsat-derived I_s and I_s trends with the determination coefficient (R^2), MAE, and bias.

2.3. Assessment of urbanization-induced impacts on I_s trends

Urbanization is often described as the increase of impervious surfaces (Gong et al., 2020; Liu et al., 2020). Here we used the impervious surface percentage (ISP, i.e., the percentage within a 1 km^2 rectangle) to investigate the urbanization-induced impacts on I_s trends. Corresponding to the I_s calculation, the urban-rural contrast in ISP (denoted as δISP) were used to represent the urbanization level, expressed by the following formula:

$$\delta\text{ISP} = ISP_{\text{urban}} - ISP_{\text{rural}} \tag{2}$$

where δISP denotes the urban-rural contrast in ISP; ISP_{urban} and ISP_{rural} denotes the urban and rural mean ISP, respectively. Analogous to the I_s trend estimation, we examined the δISP trends for each city using linear regression.

Global cities are expected to possess highly diverse expansion processes due to varying urbanization rates across cities and periods. Such contrasting urbanization processes across global cities usually lead to divergent I_s trends. To quantify the urbanization-induced impacts on I_s trends, we calculated the I_s change associated with per 1% urban land growth (denoted as β) from a temporal perspective, i.e., the slope of the linear relationship between the temporal changes in I_s and δISP (Supplementary Fig. S3). That is, we compared the β in different cities by assessing changes in I_s due to same increase in urban land proportion (i.e., δISP). The β can be calculated by:

$$\beta = \frac{\Delta I_s - b}{\Delta\delta\text{ISP}} \tag{3}$$

where ΔI_s and $\Delta\delta$ISP denote the temporal changes in I_s and δISP,

respectively; and b is a constant denoting the offset of the linear relationship between ΔI_s and $\Delta\delta$ISP. We used the static urban boundary in 2018 to assess β, mainly because it contains most of the areas experiencing rapid urbanization and can reflect the changes in δISP and the resulting changes in I_s compared to urban boundaries in earlier years.

2.4. Potential drivers of β

According to previous findings, precipitation (a climate parameter), vegetation abundance (a surface-property parameter), and population (a proxy for human activity intensity) are the main regulators on the spatial pattern of I_s (Li et al., 2019; Manoli et al., 2019; Zhao et al., 2014). We therefore also employed precipitation, vegetation abundance (rural NDVI), and urban population to investigate their roles in regulating the spatial pattern of β (i.e., urbanization-induced impacts on I_s trends) by establishing their spatial relationships across global cities. We first used ordinary correlation analysis to preliminarily examine the relationships of β with precipitation, rural NDVI, and urban population across global cities. Nevertheless, there is often co-linearity between precipitation and rural NDVI (Supplementary Figs. S4 & S5), and the role of vegetation and precipitation cannot be well differentiated in regulating β with ordinary correlation analysis. We therefore employed the partial least-squares model (i.e., a common strategy to solve co-linearity) (Wold et al., 1984) to differentiate the role of these three variables. We used the partial correlation coefficients between β and precipitation, rural NDVI, and urban population as well as the associated standardized coefficients to determine the relative importance of these three variables on regulating the spatial pattern of β across global major cities. Note that the impacts from precipitation, vegetation abundance, and urban population on β described in the study mainly reflect the controls of spatial differences in β between different cities.

2.5. Uncertainties of the method

We conducted the uncertainty analysis to examine the impacts from image number, urban definition, and factor selection on our results. First, we investigated the effects of the number difference in available Landsat images on the estimated I_s and I_s trend. This aims to examine the possible effect of the number differences in available Landsat LST across cities on the analysis associated with the I_s and I_s trend. Second, we analyzed the influence of urban definition on the magnitudes of I_s, I_s trend, and β by dividing the urban areas into urban cores (defined by the areas within the urban boundary in 1990) and urban fringes (defined as the newly expanded areas between the urban boundaries of 1990 and 2018). This analysis aims to assess the uncertainties in the estimates of I_s, I_s trend, and β caused by different urban definitions. Third, we used urban NDVI, rural NDVI, and urban-rural contrast in NDVI to detect the relationship between β and vegetation cover. This aims to analyze the effect of such factor selections on the obtained results.

3. Results

3.1. Validation of the reconstructed Landsat LST dataset

We evaluated the accuracy of the reconstruction by comparing the Landsat observations with the reconstructed LST. The results show that the mean absolute error (MAE) of the reconstructed Landsat LST is about 3 °C across global cities (Fig. 2), e.g., the MAE is 2.9 °C for one sample point in Beijing (Supplementary Fig. S2). This error may be caused by the impacts of weather system on LST. The magnitude for this error is close to that of I_s and the reliability of the reconstructed Landsat LST may therefore be doubtable in accurately portraying I_s and I_s trends. We therefore further compared the Landsat-derived I_s and I_s trends with those estimated from MODIS data for the period of 2000–2020. The comparisons show that I_s and I_s trends estimated from these two types of satellite data are in good agreement, with R^2 of 0.87 for I_s ($p < 0.001$) and R^2 of 0.55 for I_s trends ($p < 0.001$; Fig. 3b & 3d). The estimated I_s and I_s trends are also relatively consistent for individual cities (Fig. 4) and at the pixel level (e.g., Fig. 3e & 3f). When compared with those obtained from MODIS data, the mean absolute error (MAE) of the Landsat-derived I_s and I_s trends are 0.33 °C and 0.14 °C/decade, respectively. These two MAEs account for <10% of the dynamic ranges of the I_s (−4 to 5 °C) and of the associated trends (−0.7 to 1.2 °C/decade). The mean biases for the I_s and I_s trends are even lower, being equivalent to −0.10 °C and 0.01 °C/decade, respectively (Fig. 3b to 3d). These assessments indicate that the Landsat-derived I_s and I_s trends are generally reliable across global cities. The MAE of I_s and I_s trend estimates is obviously smaller than that of the reconstructed LST, probably because the I_s calculation (i.e., the difference between urban and rural mean LSTs) significantly offsets the influence of weather systems on I_s estimates (Huang et al., 2016). Note that there exist spatial differences of the estimated I_s at the pixel level (e.g., Fig. 3e & 3f) due to the differences between MODIS LST and the reconstructed Landsat LST (Supplementary Fig. S6). Such LST differences could be caused by the differences in various factors between these two types of data, such as the imaging style and LST retrieval algorithm; besides, the annual MODIS LST averages were influenced by missing data, which may cause a bias compared to the true LST values and therefore lead to the spatial difference of the estimated I_s. The final resulting annual averages of Landsat LST data at 1 km resolution for 1985–2020 are freely available at https://osf.io/qgewa/.

3.2. Global long-term I_s trends accompanied by increased urban land

From the global perspective, I_s shows a nearly linear increasing pattern since the 1980s, resembling to the growth of the urban-rural

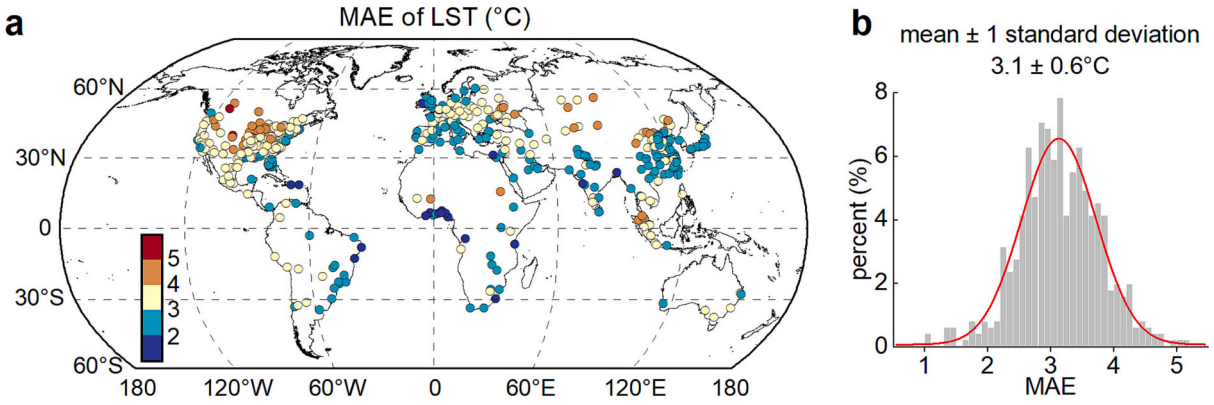

Fig. 2. The accuracy of the Prophet model for Landsat land surface temperature (LST) reconstruction across global cities. Mean absolute error (MAE) of LST reconstruction across global cities (a); and frequency histogram of MAE of LST reconstruction (b).

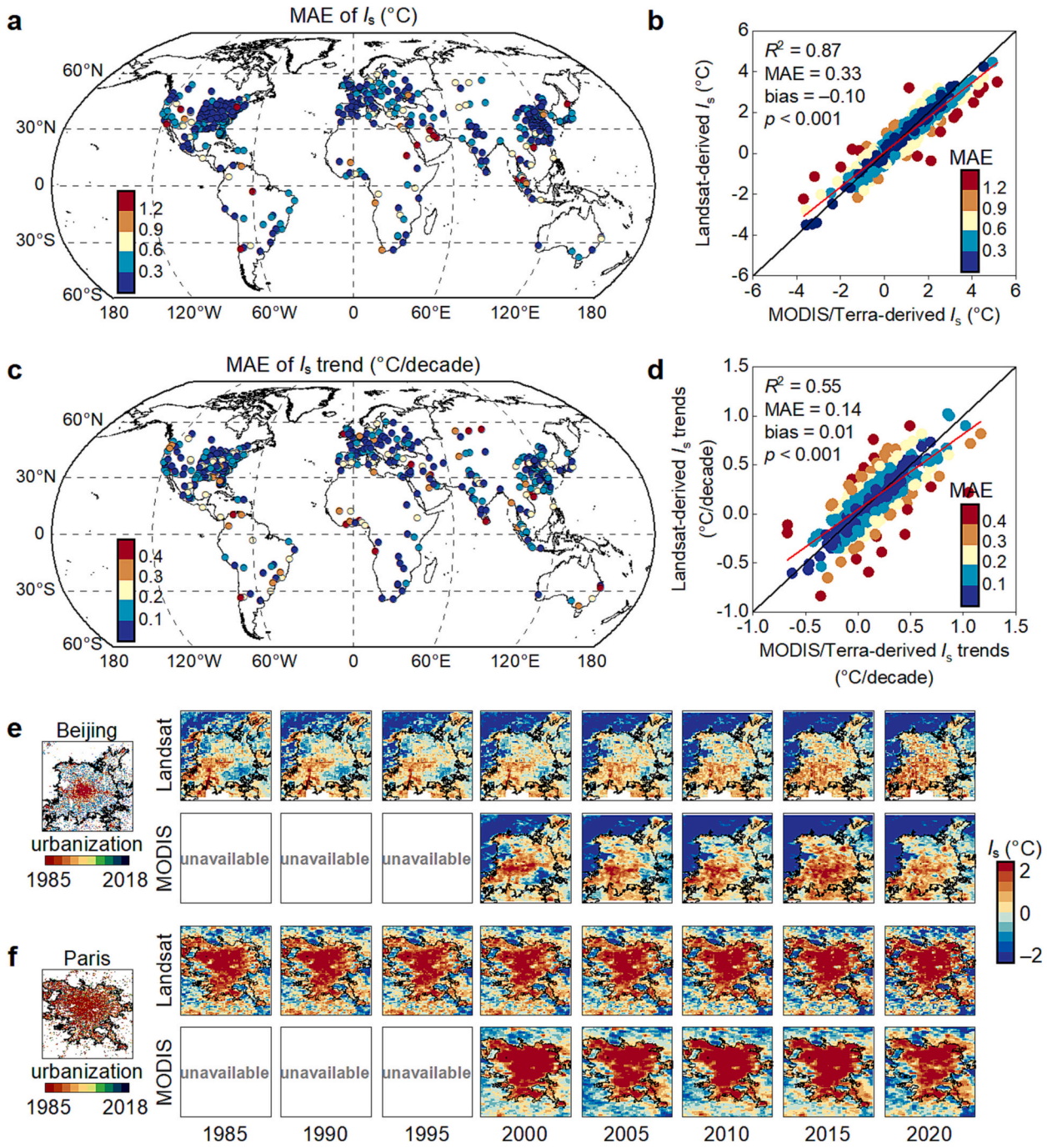

Fig. 3. Comparison of the surface urban heat island intensity (I_s) and I_s trends derived from the Landsat and MODIS annual mean thermal data. The mean absolute errors (MAEs) of the I_s (a) and I_s trends (c) across global cities; comparison of the global I_s (b) and I_s trends (d) derived from these two types of satellite data; and pixel-based comparison of the I_s over time derived from these two data sources for Beijing, China (e) and Paris, France (f), with black lines indicating the urban boundaries in 2018. The 'unavailable' label in (e) and (f) denotes the unavailability of MODIS data in these three years (1985, 1990, and 1995).

contrast in impervious surface percentage (δISP; Fig. 5a & 5b). The global mean I_s increases from 0.63 °C around 1985 to 1.14 °C in 2020, with an increasing rate of 0.156 ± 0.002 °C/decade (mean ± 95% confidence interval, $p < 0.001$), while the global mean δISP grows from 16.4% to 52.6% during the same period at a rate of 9.7 ± 0.3%/decade ($p < 0.001$). The strong temporal correlation between the I_s and δISP trends over individual cities is understandable, because urbanization (i.e., increase of δISP) significantly regulates the I_s change over time (Li et al., 2021; Li et al., 2022b). However, there is a large difference in the spatial variability of I_s and δISP growths among global cities (Fig. 5c & 5d). From the spatial perspective, the correlation between the I_s and δISP trends over global cities becomes insignificant (Fig. 5f). This implies that the more rapid urbanization rate in a city does not necessarily lead to faster I_s trends than in other cities. For example, a stagnant increase of δISP (7.7%/decade) is associated with a relatively fast increase of I_s (0.200 °C/decade) for cities in North America. While a rapid growth of δISP (15.1%/decade) is accompanied with a relatively low I_s increase (0.057 °C/decade) in African cities. Such a contrast suggests the presence of other regulators in modulating urbanization-induced impacts on I_s trends across global cities (refer to the next section for elaborate analysis).

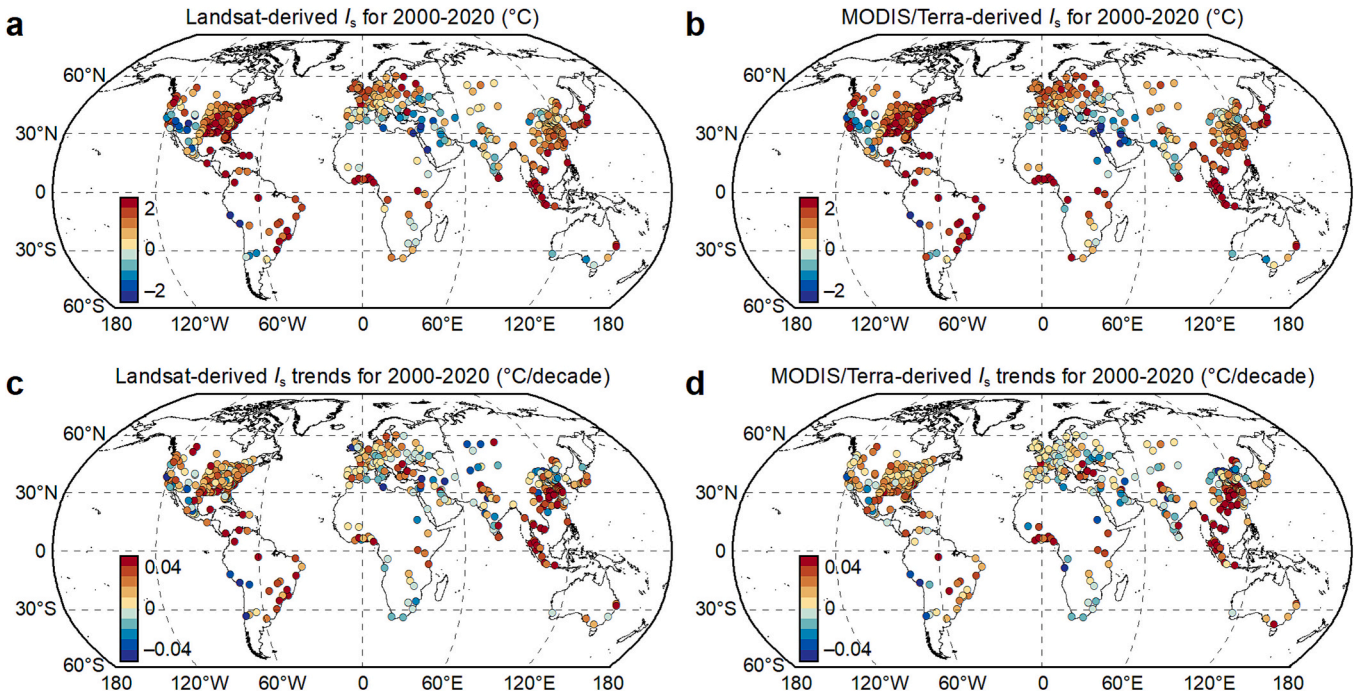

Fig. 4. Comparison of surface urban heat island intensity (I_s) and I_s trends derived from Landsat and MODIS land surface temperature (LST) data across global major cities. The mean I_s (°C) for the period of 2000–2020 derived from Landsat (a) and MODIS (b) data; the I_s trends (°C/decade) for the same period derived from Landsat (c) and MODIS (d) data.

3.3. Divergent urbanization-induced impacts on I_s trends and their regulators

The global mean β (i.e., I_s change associated with per 1% growth of δISP) is 0.018 ± 0.025 °C/% (mean ± 1 SD; Fig. 6). We find an inflection point of β on the increase of I_s along with urbanization, at which δISP is around 30%. When urban fraction δISP <30%, β remains at a rather low rate of 0.005 °C/%. As the cluster of urban areas reaches a certain density (δISP >30%), its impact on I_s triples (0.018 °C/%) (Fig. 6c). This implies urbanization can accelerate the increase of I_s as cities grow bigger or denser. This may be due to the phenomenon that urbanization is initially characterized by the occupation of bare land or areas with little vegetation, while later urban encroachment on forest land leads to a significant reduction in vegetation and accelerates the I_s growth. Moreover, the threshold for the inflection point of β varies across climate zones, generally with a smaller threshold yet larger change magnitude of β in humid climates (Fig. 7), which may be associated with greater vegetation abundance.

Regarding the spatial variations, β is greater in most cities in eastern North America, eastern South America, and Southeastern Asia, yet it is smaller in southwestern North America, western South America, central Euro-Asia, and Africa. We identified the top ten countries with the greatest β (Table S1). The identification reveals that the β is the greatest in Indonesia, followed by Brazil and the United States. In terms of climate zone, the β is the largest in equatorial zone, followed by warm temperate and then snow zones, while β is the smallest and can even be negative for many cities in arid zone. The urbanization in arid zones increases irrigation and vegetation fraction in cities than in surrounding desert environment (Fan et al., 2017; Wang, 2021), leading to a negative urbanization-induced daytime I_s and therefore a negative β.

Our analysis shows that precipitation and vegetation background are both closely related to the changing rate of I_s during the urbanization process, while the influence of urban population is negligible (Fig. 8). The β shows a non-linear relationship with precipitation (Fig. 8a). This corresponds well to previous findings that I_s correlates nonlinearly with precipitation (Manoli et al., 2019). Nevertheless, the β is more strongly related to rural normalized difference vegetation index (NDVI) compared with precipitation and urban population (Fig. 8a to 8c). Furthermore, the partial correlation coefficient of rural NDVI with β is greater than those of precipitation and urban population with β (Fig. 8d); and the standardized regression coefficient for rural NDVI is almost twice that for precipitation and is close to zero for urban population when co-explaining β ($R^2 = 0.33, p < 0.001$; Fig. 8e). This suggests that the β could be controlled mainly by rural NDVI. This finding is comparable to previous ones that I_s should be strongly regulated by evapotranspiration (Li et al., 2019), although our focus is on β (i.e., urbanization-induced impacts on the I_s trends) rather than on I_s. In fact, the strong influence of rural NDVI on the β can be intuitively understood as that, as urbanization happens over regions with more vegetation and therefore naturally higher evapotranspiration, cooling efficiency over these regions gets reduced, which leads to larger I_s. In other words, the heating potential induced by urbanization (increase of δISP) can be significantly larger over regions with abundant vegetation (mostly in humid climate) than those sparsely vegetated regions (mostly in arid climate) (Supplementary Fig. S3).

3.4. Uncertainty analysis

Several uncertainty analyses were performed on image number, urban definition, and factor selection. In terms of image number, the number of available Landsat thermal images exceeds 300 views in most cities, and the MAEs of estimated I_s and I_s trend show a slight negative correlation with image number (Supplementary Fig. S9). This indicates the disparities in the amount of available Landsat LST across cities have relatively small impacts on the analysis associated with the I_s and I_s trend. Regarding urban definition, urban cores possess significantly distinct magnitudes of I_s and I_s trends relative to urban fringes (Supplementary Fig. S10). This implies that static urban boundary does have impacts on estimation of I_s and I_s trends and may not accurately describe the magnitudes of I_s and I_s trends (or ISP) across urban categories. Nevertheless, the assessment of β is similar across urban categories; particularly, the estimated β in different urban categories is highly

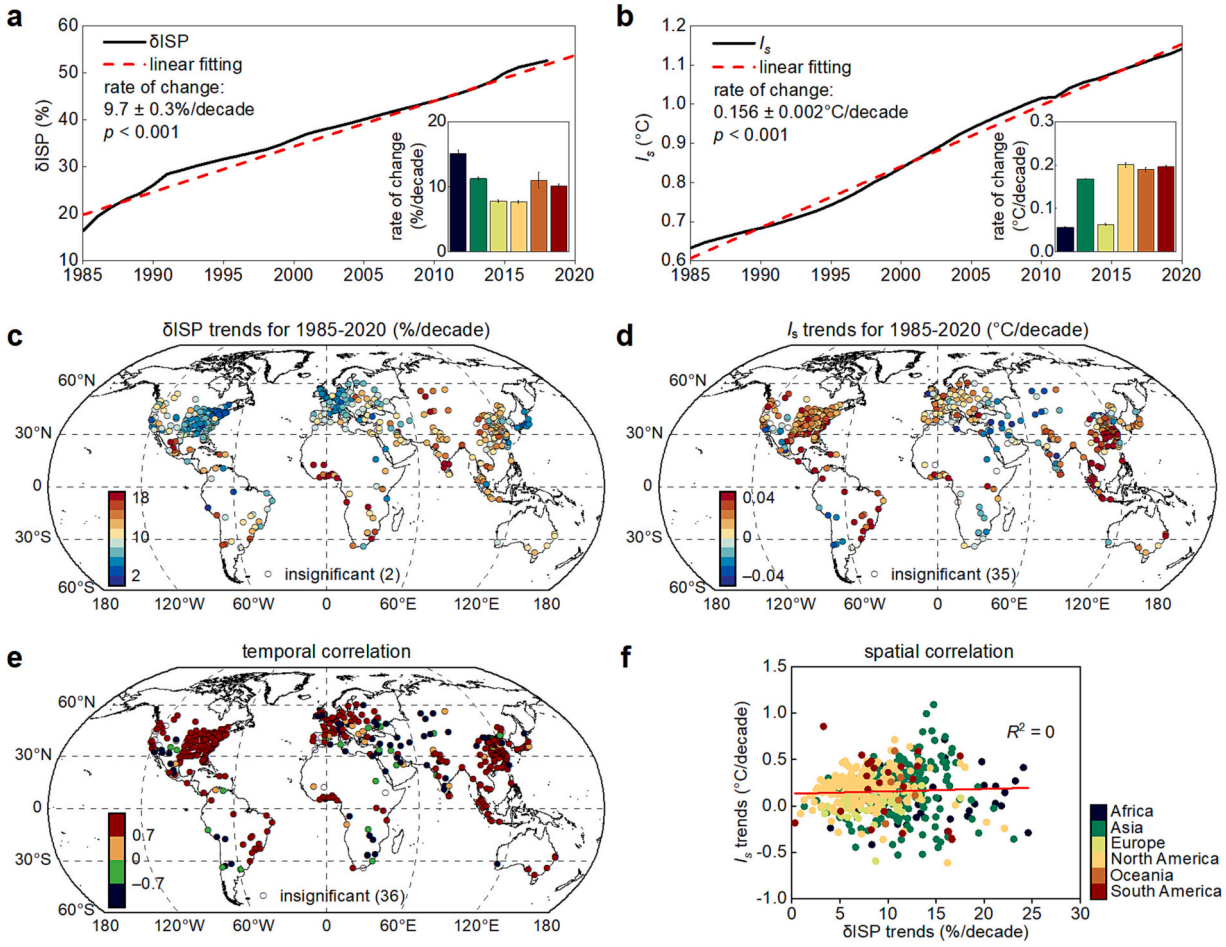

Fig. 5. The trends of urban-rural contrast in impervious surface percentage (δISP) and surface urban heat island intensity (I_s) as well as their correlations across global cities for the period of 1985–2020. The δISP trends (a) and I_s trends (b) at global and continental scales; the δISP trends (c) and I_s trends (d) for the period of 1985–2020 across global cities; the temporal correlation between δISP and I_s over time for each city (e); and the spatial correlation between δISP and I_s trends across global cities (f). Both the trend and correlation analyses are based on significance tests at the 0.05 level. The δISP and I_s trends for cities in Asia, North America, and Europe are enlarged as Supplementary Figs. S7 & S8.

correlated with that without distinguishing between urban categories, and the fitting line between the two is close to the 1:1 line (Supplementary Fig. S11). This implies that the static urban boundary used in this study should not significantly affect the estimation of β. The sensitivity analysis of factor selection shows that β is more correlated with rural NDVI compared to urban NDVI and urban-rural contrast in NDVI (Supplementary Fig. S12a to S12c). This difference in correlation may be due to larger differences in vegetation coverage among cities in rural areas than in urban areas (Supplementary Fig. S12d). The former may therefore better reflect the potential degree of urbanization-induced impacts on vegetation cover (and thus I_s change) by transforming vegetation into urban land. This indicates that our selection of rural NDVI should be appropriate for understanding the potential causes of differences in β across cities. Besides, data accuracy may also induce uncertainty in the results. For instance, the generated ISP at 1 km resolution calculated using 30 m impervious surfaces may overestimate the true ISP in urban areas; and such an overestimation may vary across cities and urban regions, therefore affecting the assessment of β. Nevertheless, such a kind of errors mainly affects the ISP magnitude and has relatively little effects on the estimates of temporal ISP trend, mainly because systematic errors can be significantly offset when fitting the overall overestimated ISP time series. That is, the effects of systematic overestimation on the slope of relationship tend to be small by fitting the relationship between overall overestimated ISP and I_s. Therefore, the overestimated ISP should not significantly affect our main findings related to β.

4. Discussion and implications

The Landsat satellites possess major advantages of global periodic and long-term observations. Several studies revealed the impacts of urbanization on I_s changes using multiple clear-sky Landsat images and land cover data (Rizvi et al., 2020; Yu et al., 2019). However, the issue of temporal discontinuity becomes a major challenge for I_s trend analysis using Landsat data due to the relatively low temporal resolution and the large amount of missing data caused by cloud cover (Ahmed et al., 2023; Zhou et al., 2019). Therefore, there may be large uncertainties associated with employing LST data from only a few time nodes to assess the impacts of urbanization on I_s trends. Several studies attempted to reconstruct Landsat (or MODIS) LST data to improve the temporal continuity of LST data to better assess the impacts of urbanization on I_s trends (Fu and Weng, 2016; Li et al., 2022b). Nevertheless, previous investigations are mainly limited to individual cities/urban agglomerations and limited to the recent two decades. A comprehensive assessment of urbanization-induced impacts on I_s trends remains lacking, especially from a global and long-term perspective. As an attempt, we reconstructed a spatiotemporally continuous LST dataset for global cities using >250,000 Landsat thermal images. We demonstrated that the reconstructed LST matches well with the MODIS LST data in quantifying I_s and its trends (Fig. 3); and the reconstructed Landsat LST data have a

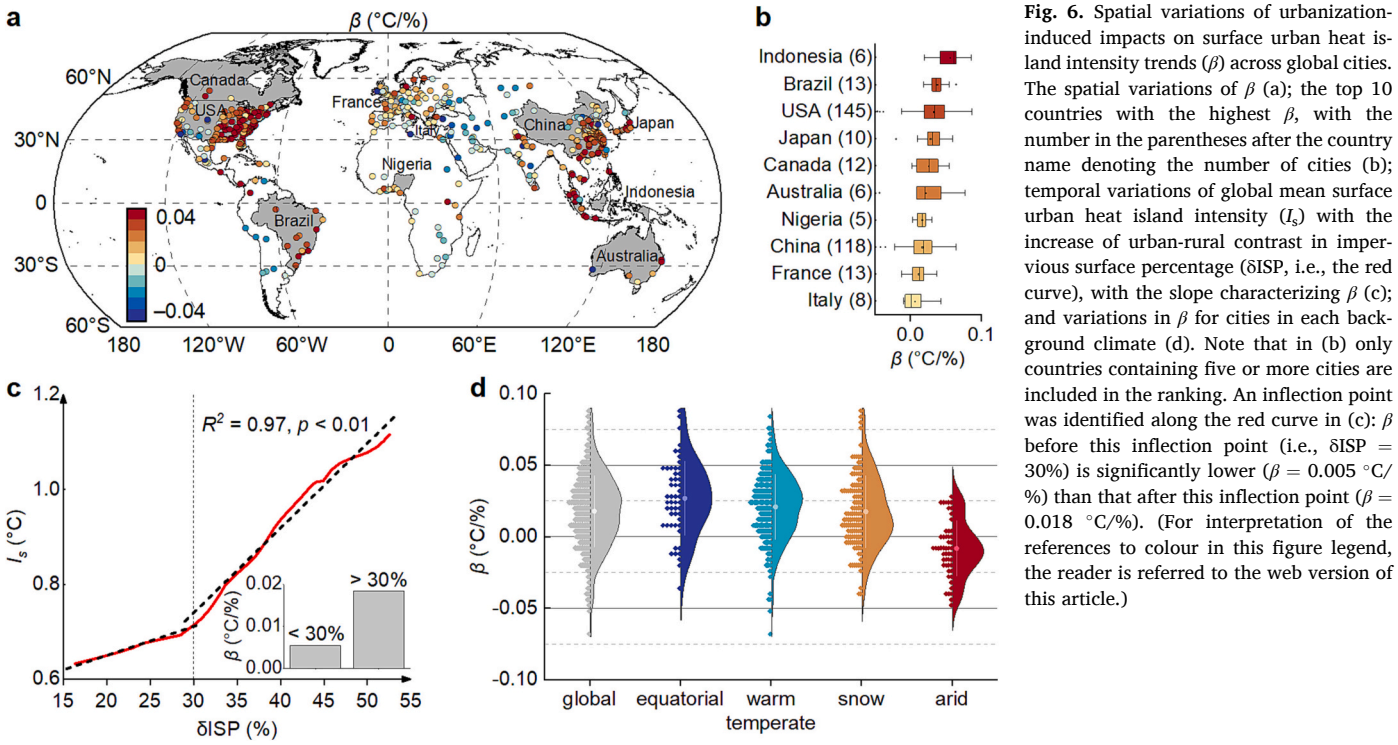

Fig. 6. Spatial variations of urbanization-induced impacts on surface urban heat island intensity trends (β) across global cities. The spatial variations of β (a); the top 10 countries with the highest β, with the number in the parentheses after the country name denoting the number of cities (b); temporal variations of global mean surface urban heat island intensity (I_s) with the increase of urban-rural contrast in impervious surface percentage (δISP, i.e., the red curve), with the slope characterizing β (c); and variations in β for cities in each background climate (d). Note that in (b) only countries containing five or more cities are included in the ranking. An inflection point was identified along the red curve in (c): β before this inflection point (i.e., δISP = 30%) is significantly lower (β = 0.005 °C/%) than that after this inflection point (β = 0.018 °C/%). (For interpretation of the references to colour in this figure legend, the reader is referred to the web version of this article.)

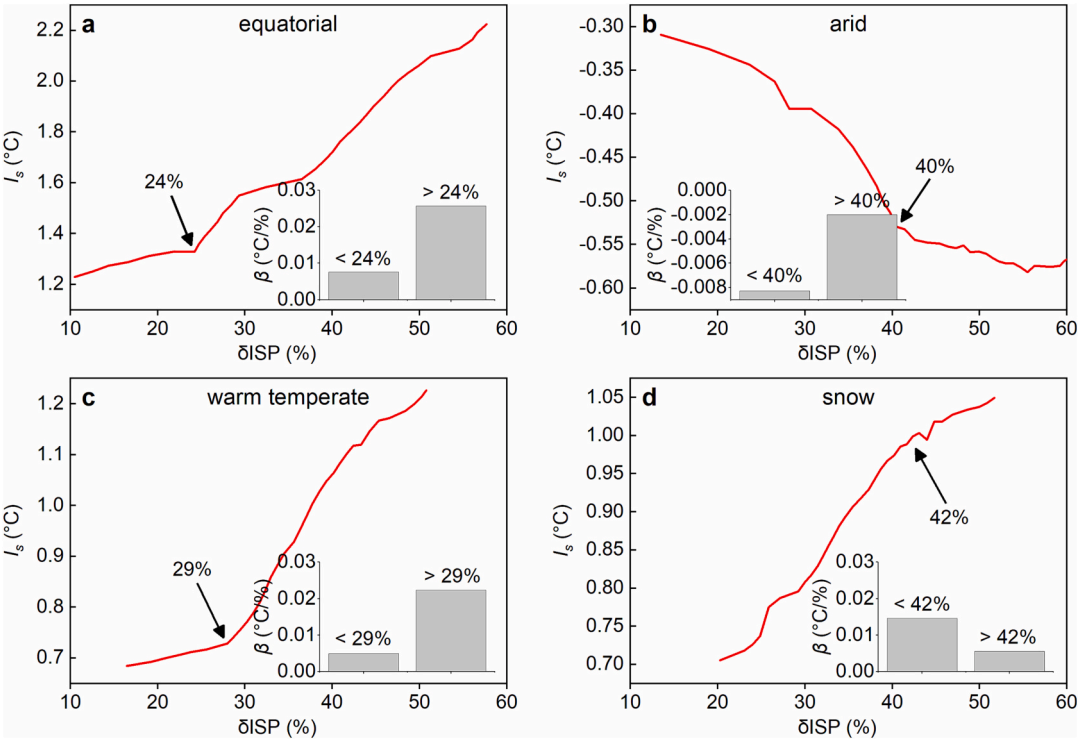

Fig. 7. Surface urban heat island intensity (I_s) variations depending on the variations in urban-rural contrast of impervious surface percentage (δISP) across climate zones, with the slopes of the red curves denoting urbanization-induced impacts on I_s trends (i.e., the β). The inflection points were identified along each red curve. There is a significant difference in the slope of the red curve (i.e., the β) before and after the inflection points. (For interpretation of the references to colour in this figure legend, the reader is referred to the web version of this article.)

high reliability for I_s analysis. We further analyzed the impacts of urbanization on long-term I_s trends by combining I_s and Landsat impervious surface data. This is perhaps the first effort to assess global I_s trends since the 1980s and to evaluate the role of urbanization in regulating such long-term trends using Landsat LST data.

The urbanization rates vary considerably across cities and during different periods (Liu et al., 2020). Such disparities in urban expansion processes may lead to significantly different I_s trends across cities and

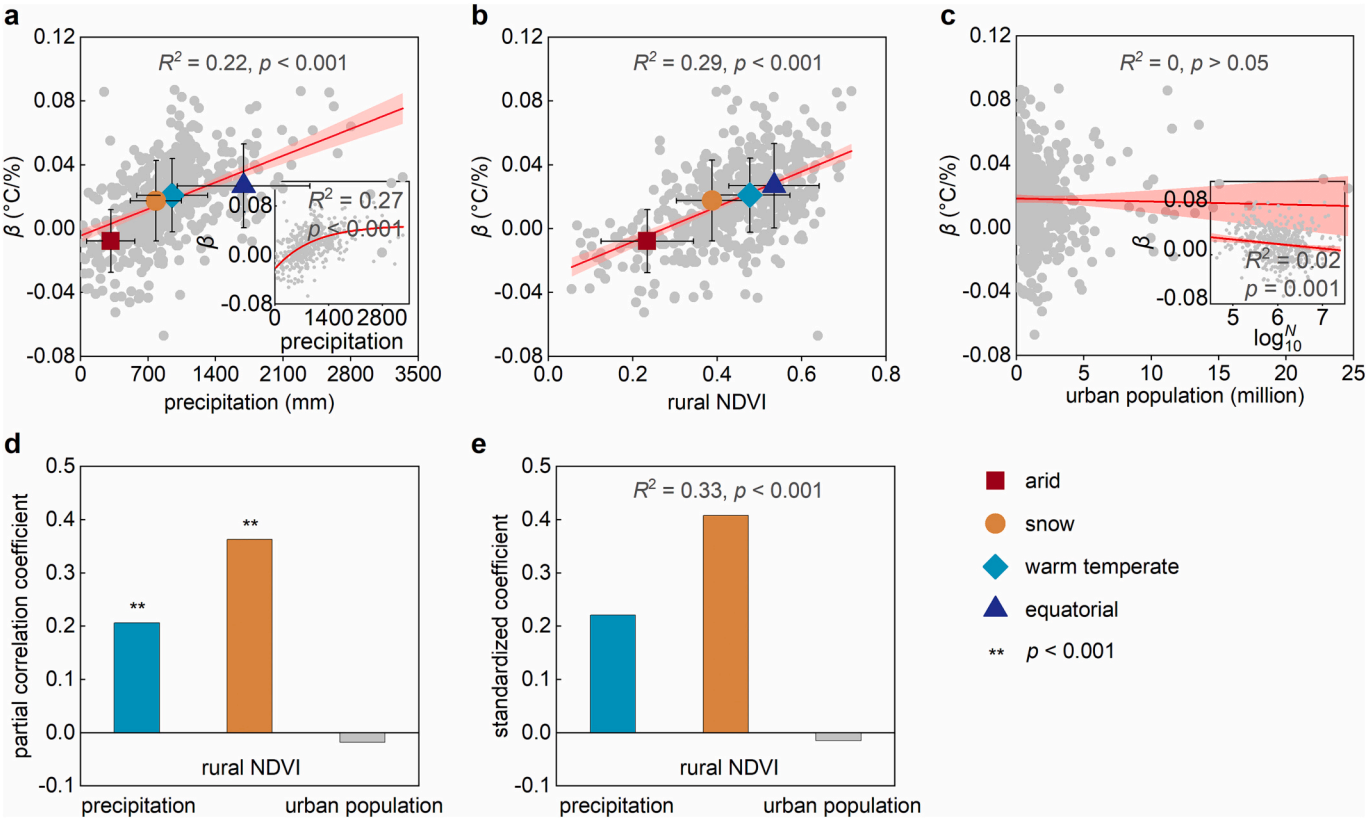

Fig. 8. Responses of urbanization-induced impacts on surface urban heat island intensity trends (β) to three factors including precipitation, rural normalized difference vegetation index (NDVI), and urban population. Correlations of β with precipitation (a), rural NDVI (b), and urban population (c); and partial correlation coefficients of β (d) and partial least-squares based standardized regression coefficients of β (e) with these three factors. The inserted subplots in (a) and (c) show the non-linear relation between β and precipitation and the relationship between β and logarithm of urban population, respectively.

periods (e.g., Supplementary Fig. S1). Accurately identifying the long-term I_s trends from a global perspective is critical to understand the impacts of urbanization on such trends. By establishing a long-term relationship between I_s and ISP in each city worldwide, we find a noteworthy 'marginal effect' of urbanization on I_s trends – the same increase of ISP can lead to significantly different amounts of I_s increase across different climates and along different urbanization stages (Figs. 6 and 7). For example, the impacts of urbanization on I_s trends are larger in humid climates (Fig. 6) that are characterized by denser vegetation and heavier precipitation (Hossain and Li, 2021; Yang et al., 2008). This implies that over cities in humid tropical regions (e.g., some African cities), urban population exposure to heat may become even more prominent in the future due to the projected increase in urban population (Rohat et al., 2019) and the notably larger I_s trends associated with urbanization (Fig. 6a). Furthermore, urbanization can impact temperature extremes (Sun et al., 2014; Wang et al., 2021; Yang et al., 2017), especially by increasing heat wave periods in humid climates (Liao et al., 2018) due to the complex interactions between UHI and temperature extremes (Zhao et al., 2018). This implies that urban population exposure to extreme heat events can therefore be further augmented over humid cities due to urbanization. We also find an evident threshold for the urbanization-induced impacts on I_s trends, e.g., the I_s trends can accelerate when urban impervious land exceeds 30% (Fig. 6c). The enhanced impacts of urbanization with the proportion of urban impervious land may be associated with the increasing magnitude of the reduction in evapotranspiration due to local urbanization (Zhou et al., 2022). This implies that the increase in heat exposure of urban residents may be amplified with the advance of urbanization. Special care should therefore be taken on such a threshold in sustainable urban planning, although this threshold may change for individual cities (Fig. 7). Besides, previous studies interestingly showed that surface temperatures are higher in regions near barren land and lower in those close to vegetation and water bodies, described as the 'proximity effect' (Mansourmoghaddam et al., 2021; Mansourmoghaddam et al., 2023). Here we further find that cities with larger I_s (or I_s trend) in urban cores also have stronger I_s (or I_s trend) in urban fringes (Supplementary Fig. S10). This implies that the 'proximity effect' exists not only between small urban patches (e.g., barren land, vegetated areas and water bodies) and their surroundings, but may also occur among regional urban thermal environments at a larger spatial scale. This finding indicates that the 'proximity effect' needs to be considered in the design of future urban heat mitigation strategies to hinder the effects of urbanization-induced rapid surface warming on the surrounding thermal environment.

Satellite thermal data with high spatial resolution are required to better understand inner-city I_s changes and their controlling factors (Sobrino et al., 2012). Compared to reanalysis data and other satellite data (e.g., MODIS and AVHRR LSTs), Landsat LST data have a much higher spatial resolution, enabling the monitoring of thermal environmental characteristics at the landscape scale. However, due to the huge computational burden involved in reconstructing 100-m Landsat LST, here we only reconstructed the Landsat LST dataset for 1985–2020 at 1-km spatial resolution, as our primary purpose is to assess the impacts of global urbanization on long-term I_s trends at the city scale. Our method should be able to reconstruct 100-m Landsat LST if the computational capacity permits. This implies that our approach should be useful to assess local thermal environmental changes and their responses to urban landscape or landscape change from a fine-scale perspective for future studies. For example, the Landsat LST reconstruction method may help better assess the long-term and fine-scale changes in urban thermal environments (Li et al., 2022a), the impacts of land cover change on

surface temperatures (Fu and Weng, 2016), as well as identify the cooling and heating effects of blue-green space (Gunawardena et al., 2017) and industrial plants (Gao et al., 2022) on their surroundings, respectively.

Previous studies have revealed urbanization-induced impacts on the evolution of the urban thermal environment (Li et al., 2021; Li et al., 2022b; Sun et al., 2014; Wang et al., 2021; Yang et al., 2017) and assessed the relative importance of controlling factors of I_s (Lai et al., 2021; Li et al., 2019). While urbanization-induced vegetation reduction is traditionally considered as the dominant factor affecting I_s (Peng et al., 2012; Zhou et al., 2014), background precipitation and urban population have been also shown to exert a strong control (Manoli et al., 2019; Zhao et al., 2014). Nevertheless, studies that found strong control of background precipitation are not contradictory to those that stressed the control of vegetation, because the rural vegetation depend strongly on background precipitation (Supplementary Fig. S5). This is analogous to previous findings from a spatial perspective that the change trends of LST with increasing impervious surface percentage are largely regulated by both evapotranspiration and background precipitation (Zhou et al., 2022). Here, by differentiating the relative importance of rural vegetation, precipitation, and urban population based on partial least-squares model, we further find that while such urbanization-induced impacts on I_s trends are closely related to the background precipitation where cities are located, they are more strongly induced by differences in vegetation abundance (Fig. 8). We therefore provide evidence that, resembling the absolute I_s, the I_s trends could be more influenced by vegetation abundance relative to background precipitation and urban population. Our study thus highlights the potential of urban green spaces as an effective strategy to reduce I_s growth during the urbanization process.

Credit author statement

W. Zhan and L. Li conceived and designed project. L. Li performed data analysis. L. Li and W. Zhan wrote manuscript. D. Wang provides technical assistance in data reconstruction. L. Hu, T. Chakraborty, Z. Wang, P. Fu, W. Liao, F. Huang, H. Fu, J. Li, Z. Liu, H. Du, and S. Wang contributed ideas to data analysis, results interpretation, and manuscript revision. All authors have read and approved the paper.

Declaration of Competing Interest

The authors declare that they have no known competing financial interests or personal relationships that could have appeared to influence the work reported in this paper.

Data availability

Data will be made available on request.

Acknowledgements

We gratefully acknowledge the following organizations for providing the funding to support this study, including the National Natural Science Foundation of China (no. 42171306 and 42001270) and the Postgraduate Research & Practice Innovation Program of Jiangsu Province (no. KYCX22_0112). We also thank the support from the National Youth Talent Support Program of China. T. Chakraborty's contribution was supported by COMPASS-GLM, a multi-institutional project supported by the U.S. Department of Energy, Office of Science, Office of Biological and Environmental Research as part of the Earth and Environmental Systems Modeling program. PNNL is operated for the Department of Energy by Battelle Memorial Institute under contract DE-AC05-76RL01830.

Appendix A. Supplementary data

Supplementary data to this article can be found online at https://doi.org/10.1016/j.rse.2023.113650.

References

Ahmed, M.R., Ghaderpour, E., Gupta, A., Dewan, A., Hassan, Q.K., 2023. Opportunities and challenges of spaceborne sensors in delineating land surface temperature trends: a review. IEEE Sensors J. 23, 6460–6472.
Chakraborty, T.C., Lee, X., 2019. A simplified urban-extent algorithm to characterize surface urban heat islands on a global scale and examine vegetation control on their spatiotemporal variability. Int. J. Appl. Earth Obs. 74, 269–280.
Chakraborty, T.C., Lee, X., Ermida, S., Zhan, W., 2021. On the land emissivity assumption and landsat-derived surface urban heat islands: a global analysis. Remote Sens. Environ. 265, 112682.
Dewan, A., Kiselev, G., Botje, D., Mahmud, G.I., Bhuian, M.H., Hassan, Q.K., 2021. Surface urban heat island intensity in five major cities of Bangladesh: patterns, drivers and trends. Sustain. Cities Soc. 71, 102926.
Ermida, S.L., Mantas, V., Trigo, I.F., 2020. Google earth engine open-source code for land surface temperature estimation from the landsat series. Remote Sens-Basel 12 (9), 1471.
Fan, C., Myint, S.W., Kaplan, S., Middel, A., Zheng, B., Rahman, A., Huang, H.P., Brazel, A.J., Blumberg, D.G., 2017. Understanding the impact of urbanization on surface urban heat islands—A longitudinal analysis of the oasis effect in subtropical desert cities. Remote Sens-Basel 9 (7), 672.
Fu, P., Weng, Q., 2016. A time series analysis of urbanization induced land use and land cover change and its impact on land surface temperature with landsat imagery. Remote Sens. Environ. 175, 205–214.
Gao, J., Meng, Q., Zhang, L., Hu, D., 2022. How does the ambient environment respond to the industrial heat island effects? An innovative and comprehensive methodological paradigm for quantifying the varied cooling effects of different landscapes. GISci. Remote Sens. 59 (1), 1643–1659.
Gong, P., Li, X., Wang, J., Bai, Y., Chen, B., Hu, T., Liu, X., Xu, B., Yang, J., Zhang, W., Zhou, Y., 2020. Annual maps of global artificial impervious area (GAIA) between 1985 and 2018. Remote Sens. Environ. 236, 111510.
Gunawardena, K.R., Wells, M.J., Kershaw, T., 2017. Utilising green and bluespace to mitigate urban heat island intensity. Sci. Total Environ. 584, 1040–1055.
Huang, F., Zhan, W., Voogt, J., Hu, L., Wang, Z., Quan, J., Ju, W., Guo, Z., 2016. Temporal upscaling of surface urban heat island by incorporating an annual temperature cycle model: a tale of two cities. Remote Sens. Environ. 186, 1–12.
Hossain, M.L., Li, J., 2021. NDVI-based vegetation dynamics and its resistance and resilience to different intensities of climatic events. Glob. Ecol. Conserv. 30, e01768.
Imhoff, M.L., Zhang, P., Wolfe, R.E., Bounoua, L., 2010. Remote sensing of the urban heat island effect across biomes in the continental USA. Remote Sens. Environ. 114 (3), 504–513.
Kalnay, E., Cai, M., 2003. Impact of urbanization and land-use change on climate. Nature 423, 528–531.
Kottek, M., Grieser, J., Beck, C., Rudolf, B., Rubel, F., 2006. World map of the Köppen-Geiger climate classification updated. Meteorol. Z. 15, 259–263.
Lai, J., Zhan, W., Quan, J., Liu, Z., Li, L., Huang, F., Hong, F., Liao, W., 2021. Reconciling debates on the controls on surface urban Heat Island intensity: effects of scale and sampling. Geophys. Res. Lett. 48 (19), e2021GL094485.
Lehmann, R., 2013. 3 σ-rule for outlier detection from the viewpoint of geodetic adjustment. J. Surv. Eng. 139 (4), 157–165.
Li, D., Liao, W., Rigden, A.J., Liu, X., Wang, D., Malyshev, S., Shevliakova, E., 2019. Urban heat island: Aerodynamics or imperviousness? Sci. Adv. 5 (4), eaau4299.
Li, J., Zhan, W., Hong, F., Lai, J., Dong, P., Liu, Z., Wang, C., Huang, F., Li, L., Wang, C., Fu, Y., Miao, S., 2021. Similarities and disparities in urban local heat islands responsive to regular-, stable-, and counter-urbanization: A case study of Guangzhou, China. Build. Environ. 199, 107935.
Li, L., Zha, Y., Zhang, J., Li, Y., Lyu, H., 2020. Using prophet forecasting model to characterize the temporal variations of historical and future surface urban heat island in China. J. Geophys. Res. Atmos. 125, e2019JD031968.
Li, L., Zhan, W., Du, H., Lai, J., Wang, C., Fu, H., Huang, F., Liu, Z., Wang, C., Li, J., Jiang, L., Miao, S., 2022a. Long-term and fine-scale surface urban Heat Island dynamics revealed by landsat data since the 1980s: a comparison of four megacities. J. Geophys. Res. Atmos. 127 (5), e2021JD035598.
Li, H., Zhou, Y., Jia, G., Zhao, K., Dong, J., 2022b. Quantifying the response of surface urban heat island to urbanization using the annual temperature cycle model. Geosci. Front. 13 (1), 101141.
Li, X., Gong, P., Zhou, Y., Wang, J., Bai, Y., Chen, B., Hu, T., Xiao, Y., Xu, B., Yang, J., Liu, X., Cai, W., Huang, H., Wu, T., Wang, X., Lin, P., Li, X., Chen, J., He, C., Li, X., Yu, L., Clinton, N., Zhu, Z., 2020. Mapping global urban boundaries from the global artificial impervious area (GAIA) data. Environ. Res. Lett. 15, 094044.
Liao, W., Liu, X., Li, D., Luo, M., Wang, D., Wang, S., Baldwin, J., Lin, L., Li, X., Feng, K., Klaus, H., Yang, X., 2018. Stronger contributions of urbanization to heat wave trends in wet climates. Geophys. Res. Lett. 45 (20), 11–310.
Liu, X., Huang, Y., Xu, X., Li, X., Li, X., Ciais, P., Lin, P., Gong, K., Ziegler, A.D., Chen, A., Gong, P., Chen, J., Hu, G., Chen, Y., Wang, S., Wu, Q., Huang, K., Estes, L., Zeng, Z., 2020. High-spatiotemporal-resolution mapping of global urban change from 1985 to 2015. Nat. Sustain. 3, 564–570.

Manoli, G., Fatichi, S., Schläpfer, M., Yu, K., Crowther, T.W., Meili, N., Burlando, P., Katul, G.G., Bou-Zeid, E., 2019. Magnitude of urban heat islands largely explained by climate and population. Nature 573 (7772), 55–60.
Mansourmoghaddam, M., Rousta, I., Zamani, M., Mokhtari, M.H., Karimi Firozjaei, M., Alavipanah, S.K., 2021. Study and prediction of land surface temperature changes of Yazd city: assessing the proximity and changes of land cover. J. RS GIS Nat. Resour. 12 (4), 1–27.
Mansourmoghaddam, M., Rousta, I., Zamani, M., Olafsson, H., 2023. Investigating and predicting Land Surface Temperature (LST) based on remotely sensed data during 1987–2030 (A case study of Reykjavik city, Iceland). Urban Ecosyst. https://doi.org/10.1007/s11252-023-01337-9.
Meng, Q., Zhang, L., Sun, Z., Meng, F., Wang, L., Sun, Y., 2018. Characterizing spatial and temporal trends of surface urban heat island effect in an urban main built-up area: A 12-year case study in Beijing, China. Remote Sens. Environ. 204, 826–837.
Oke, T., 1982. The energetic basis of the urban heat island. Q. J. R. Meteorol. Soc. 108 (455), 1–24.
Peng, S., Piao, S., Ciais, P., Friedlingstein, P., Ottle, C., Breon, F.M., Nan, H., Zhou, L., Myneni, R.B., 2012. Surface urban heat island across 419 global big cities. Environ. Sci. Technol. 46 (2), 696–703.
Qian, Y., Chakraborty, T.C., Li, J., Li, D., He, C., Sarangi, C., Chen, F., Yang, X., Leung, L. R., 2022. Urbanization impact on regional climate and extreme weather: current understanding, uncertainties, and future research directions. Adv. Atmos. Sci. 1–42.
Quan, J., Zhan, W., Chen, Y., Wang, M., Wang, J., 2016. Time series decomposition of remotely sensed land surface temperature and investigation of trends and seasonal variations in surface urban heat islands. J. Geophys. Res. Atmos. 121 (6), 2638–2657.
Rizvi, S.H., Fatima, H., Iqbal, M.J., Alam, K., 2020. The effect of urbanization on the intensification of SUHIs: analysis by LULC on Karachi. J. Atmos Sol.-Terr. Phys. 207, 105374.
Rohat, G., Flacke, J., Dosio, A., Dao, H., van Maarseveen, M., 2019. Projections of human exposure to dangerous heat in african cities under multiple socioeconomic and climate scenarios. Earths Future 7 (5), 528–546.
Si, M., Li, Z.L., Nerry, F., Tang, B.H., Leng, P., Wu, H., Zhang, X., Shang, G., 2022. Spatiotemporal pattern and long-term trend of global surface urban heat islands characterized by dynamic urban-extent method and MODIS data. ISPRS J. Photogramm. 183, 321–335.
Sobrino, J., Oltra-Carrió, R., Sòria, G., Bianchi, R., Paganini, M., 2012. Impact of spatial resolution and satellite overpass time on evaluation of the surface urban heat island effects. Remote Sens. Environ. 117, 50–56.
Sun, Y., Zhang, X., Zwiers, F.W., Song, L., Wan, H., Hu, T., Yin, H., Ren, G., 2014. Rapid increase in the risk of extreme summer heat in eastern China. Nat. Clim. Chang. 4 (12), 1082–1085.
Taylor, S.J., Letham, B., 2018. Forecasting at scale. Am. Stat. 72 (1), 37–45.
Tran, D.X., Pla, F., Latorre-Carmona, P., Myint, S.W., Caetano, M., Kieu, H.V., 2017. Characterizing the relationship between land use land cover change and land surface temperature. ISPRS J. Photogramm. 124, 119–132.
UNEP, 2021. Beating the Heat: A Sustainable Cooling Handbook for Cities. Nairobi.
Wan, Z., 2008. New refinements and validation of the MODIS land-surface temperature/emissivity products. Remote Sens. Environ. 112 (1), 59–74.
Wang, J., Chen, Y., Liao, W., He, G., Tett, S.F., Yan, Z., Zhai, P., Feng, J., Ma, W.J., Huang, C., Hu, Y., 2021. Anthropogenic emissions and urbanization increase risk of compound hot extremes in cities. Nat. Clim. Chang. 12, 11.
Wang, Z.H., 2021. Compound environmental impact of urban mitigation strategies: co-benefits, trade-offs, and unintended consequence. Sustain. Cities Soc. 75, 103284.
Wold, S., Ruhe, A., Wold, H., Dunn, W.J., 1984. The collinearity problem in linear regression. The partial least squares (PLS) approach to generalized inverses. SIAM J. Sci. Comput. 5 (3), 735–743.
Yang, X., Ruby, L.L., Zhao, N., Zhao, C., Qian, Y., Hu, K., Liu, X., Baode, C., 2017. Contribution of urbanization to the increase of extreme heat events in an urban agglomeration in East China. Geophys. Res. Lett. 44 (13), 6940–6950.
Yang, Y., Fang, J., Ma, W., Wang, W., 2008. Relationship between variability in aboveground net primary production and precipitation in global grasslands. Geophys. Res. Lett. 35 (23), L23710.
Yao, R., Wang, L., Huang, X., Zhang, W., Li, J., Niu, Z., 2018. Interannual variations in surface urban heat island intensity and associated drivers in China. J. Environ. Manag. 222, 86–94.
Yao, R., Wang, L., Huang, X., Gong, W., Xia, X., 2019. Greening in rural areas increases the surface urban heat island intensity. Geophys. Res. Lett. 46 (4), 2204–2212.
Yu, Z., Yao, Y., Yang, G., Wang, X., Vejre, H., 2019. Spatiotemporal patterns and characteristics of remotely sensed region heat islands during the rapid urbanization (1995–2015) of southern China. Sci. Total Environ. 674, 242–254.
Zhao, L., Lee, X., Smith, R.B., Oleson, K., 2014. Strong contributions of local background climate to urban heat islands. Nature 511 (7508), 216–219.
Zhao, L., Oppenheimer, M., Zhu, Q., Baldwin, J.W., Ebi, K.L., Bou-Zeid, E., Guan, K., Liu, X., 2018. Interactions between urban heat islands and heat waves. Environ. Res. Lett. 13 (3), 034003.
Zhou, D., Zhao, S., Liu, S., Zhang, L., Zhu, C., 2014. Surface urban heat island in China's 32 major cities: spatial patterns and drivers. Remote Sens. Environ. 152, 51–61.
Zhou, D., Xiao, J., Bonafoni, S., Berger, C., Deilami, K., Zhou, Y., Frolking, S., Yao, R., Qiao, Z., Sobrino, J.A., 2019. Satellite remote sensing of surface urban heat islands: Progress, challenges, and perspectives. Remote Sens-Basel 11 (1), 48.
Zhou, D., Xiao, J., Frolking, S., Zhang, L., Zhou, G., 2022. Urbanization contributes little to global warming but substantially intensifies local and regional land surface warming. Earth's. Future 10 (5), e2021EF002401.